

Optics Letters

Split-spectrum dual-domain phase-intensity fusion optical coherence tomography angiography

HONGTAO WEI,^{1,2} FUWANG WU,^{1,2} XIAOQI LU,^{1,2} KAIXUAN HU,^{1,2} D ZHENGKAI YAO,^{1,2} LEI ZHANG,^{1,2} AND WEIYE SONG^{1,2,*} D

Received 27 June 2025; revised 30 September 2025; accepted 8 October 2025; posted 9 October 2025; published 6 November 2025

Optical coherence tomography angiography (OCTA) provides micrometer-resolution maps of the retinal microvasculature. However, even slight ocular motion can introduce pronounced motion artifacts that degrade image quality. To overcome this, we present a split-spectrum dual-domain phase-intensity fusion algorithm. The approach mitigates low-frequency phase drift in the time domain, corrects systematic phase errors in the frequency domain, and integrates complementary amplitude-decorrelation and phasedifference information. Independent processing of spectral sub-bands further enhances the flow signal-to-noise ratio. In vivo mouse-retina imaging shows that, even without additional inter-frame registration, the method markedly improves angiographic contrast and signal fidelity while greatly reducing motion artifacts. This technique provides a reliable path to high-quality OCTA under dynamic conditions or at low acquisition frame rates. © 2025 Optica Publishing Group. All rights, including for text and data mining (TDM), Artificial Intelligence (AI) training, and similar technologies, are reserved.

https://doi.org/10.1364/OL.572090

Optical coherence tomography angiography (OCTA) extends optical coherence tomography (OCT) by mapping retinal microvasculature through the motion contrast of red blood cells [1,2]. Its label-free and non-invasive operation supports early diagnosis of glaucoma, age-related macular degeneration, diabetic retinopathy, and other vasculopathies [3–5]. During in vivo acquisition, however, cardiac and respiratory cycles disturb the OCT interferogram, producing phase jitter that appears as vessel discontinuities and motion artifacts, undermining diagnostic confidence and limiting longitudinal studies in pre-clinical models [6,7]. The impact is particularly severe for high-speed volumetric scans, where fewer repeated frames are available for averaging and traditional motion correction tends to break down.

Inter-frame image registration is the standard remedy for these artifacts [8,9], but it adds a dedicated post-processing stage, demands substantial memory bandwidth. Among the motion-contrast algorithms reported to date, three remain highly influential. Speckle-variance OCTA (SVOCT) evaluates

pixel-wise intensity variance across repeated frames to highlight moving scatterers [10]. Optical microangiography (OMAG) extracts flow contrast from complex-signal amplitude and phase differences between successive B-scans [11]. Split-spectrum amplitude-decorrelation angiography (SSADA) partitions the interferogram into narrow sub-bands and computes intensity decorrelation in each band to improve flow sensitivity [12]. Despite their proven utility, all three algorithms operate almost exclusively in the time domain and therefore under-utilise frequency-domain phase information. High-frequency artifacts driven by ocular tremor or cardiac pulsation are only partially suppressed, which has become a bottleneck for further gains in image fidelity.

We introduce a split-spectrum, dual-domain phase-intensity fusion (SSDDPIF) algorithm that reduces dependence on registration while attenuating artifacts over a broad frequency band. Consecutive B-scan phases are first aligned in the time domain to cancel eye-motion-induced low-frequency drift, then the data are converted to the frequency domain where residual heartbeatrelated fluctuations are compensated axially and laterally [13]. Amplitude-decorrelation and phase-difference cues are subsequently fused: amplitude contrast accentuates fast flow in large retinal vessels whereas phase contrast detects slow capillary flow, thereby expanding the measurable velocity range [14]. A final split-spectrum step divides the interferogram into multiple bands and processes phase and amplitude independently in each [12], boosting flow signal-to-noise ratio and suppressing lingering artifacts. We implemented this SSDDPIF on a 250 kHz spectral-domain OCT system and quantitatively compared its performance with OMAG, SVOCT, and SSADA.

In this study, we used a custom-built spectral-domain OCT (SD-OCT) system to acquire OCTA data. The light source utilized was a superluminescent diode (SLD) with a central wavelength of 853.5 nm and a spectral bandwidth of 145 nm. The detector was a high-speed line-scan camera (Octoplus, e2v, Teledyne, UK). The axial resolution of the system was approximately 2.3 μm , and at a sample depth of 1.2 mm, the signal strength rolloff was about 5.7 dB, with a roll-off of approximately 11.88 dB at 2 mm. When the A-scan rate is 250 kHz, the sensitivity of the system is about 99.95 dB [15].

The scan consisted of K lateral positions (i.e., B-scan positions), with N B-scans acquired at each position. The resulting

¹School of Mechanical Engineering, Shandong University, Shandong Jinan 250061, China

²Key Laboratory of High Efficiency and Clean Mechanical Manufacture of Ministry of Education, Shandong University, Shandong Jinan 250061, China

^{*}songweiye@sdu.edu.cn

three-dimensional data dimensions are (i, j, n, and k), where i represents the depth direction pixel index (A-scan sampling points), j represents the lateral pixel index (within the B-scan position), n = 1, 2, ..., N represents the frame number at the same position k, and k = 1, 2, ..., K represents the lateral position number of the B-scan.

First, a fixed B-scan position k was selected in the 3D data, and the n-th frame and the n+1-th frame of B-scan complex signals (n = 1, 2, ..., N-1) adjacent to this position were extracted. Using these two frames of complex OCT signals, we computed the global phase shift $\Delta\phi_{\rm time}(n)$ between them by conjugate multiplication to estimate the overall phase shift due to respiration or heartbeat, etc. The global phase offset $\Delta\phi_{\rm time}(n)$ was obtained by multiplying the n+1-th frame signal pixel-by-pixel by the conjugate value of the n-th frame signal, and then averaging the resulting phase difference in the B-scan plane. Deducting this offset from the complex signal of the n+1-th frame, i.e., multiplying it by the phase correction factor $\exp[-i\Delta\phi_{\rm time}(n)]$, completed the time-domain phase correction of the n+1-th frame with respect to the n-th frame.

$$\Delta \phi_{\text{time}} = -\frac{1}{M} \tan^{-1} \left(\frac{\text{Im} \left(\sum_{i=1}^{M} B_{i,j,n+1} B_{i,j,n}^{*} \right)}{\text{Re} \left(\sum_{i=1}^{M} B_{i,j,n+1} B_{i,j,n}^{*} \right)} \right). \tag{1}$$

After this frame-by-frame correction, the time domain corrected B-scan data $B_{i,j,n+1}^{(t)}$ (t means time domain corrected) was updated. Equation (2) represents the process of time domain phase correction:

$$B_{i,i,n+1}^{(t)} = B_{i,j,n+1} \exp \left[-i\Delta \phi_{\text{time}} (n) \right].$$
 (2)

Despite this correction, high-frequency phase noise due to micro-scale tissue vibrations often persists. Therefore, a further correction was performed in the frequency domain. To further eliminate the residual artifacts, we converted the corrected B-scan signals to the frequency domain for processing. A two-dimensional Fourier transform was applied to the time-corrected data $B_{i,l,n}^{(t)}$ for each frame:

$$B_{u,v,n} = FFT_{i,i} \left\{ B_{i,i,n+1}^{(t)} \right\},$$
 (3)

where u and v denote the spatial frequency components corresponding to the depth direction (i) and lateral B-scan direction (j), respectively. In the frequency-domain representation, the low-frequency components with v close to 0 usually reflect slowly changing or static tissue signals, whereas the higher v components are more likely to come from rapidly changing signals due to blood flow. We estimate the corresponding phase-corrected distribution $\Delta\Phi_{\rm freq}(u,v,n)$ in the frequency domain to compensate for the frequency-domain phase error caused by tissue micro-motion. The frequency domain signal after correction is expressed as:

$$\Delta \phi_{\text{freq}} = -\frac{1}{u} \tan^{-1} \left(\frac{\text{Im} \left(\sum_{u=1}^{U} B_{u,v,n+1} B_{u,v,n}^* \right)}{\text{Re} \left(\sum_{u=1}^{U} B_{u,v,n+1} B_{u,v,n}^* \right)} \right).$$
 (4)

With the frequency domain phase correction, we obtained the corrected frequency domain signal:

$$B'_{u,v,n} = B_{u,v,n+1} \exp\left[-i\Delta\phi_{\text{freq}}(u,v,n)\right].$$
 (5)

Then a two-dimensional inverse Fourier transform was applied to obtain the frequency-domain phase-corrected time-domain signal $B_{i,j,n}^{(\text{corrected})}$.

Subsequently, using these fully corrected frames, we calculated intensity and phase differences to characterize blood flow. The intensity difference (ID) was computed as:

$$ID_{i,j,n} = \left| B_{i,j,n+1}^{\text{(corrected)}} - B_{i,j,n}^{\text{(corrected)}} \right|,$$
 (6)

which captures amplitude fluctuations caused by blood flow. Concurrently, the local phase difference $\phi'_{i,j,n}$ was calculated using the complex product of adjacent corrected frames:

$$\phi'_{i,j,n} = \tan^{-1} \left(\frac{\operatorname{Im} \left[B_{i,j,n+1}^{(corrected)} \left(B_{i,j,n}^{(corrected)} \right)^* \right]}{\operatorname{Re} \left[B_{i,j,n+1}^{(corrected)} \left(B_{i,j,n}^{(corrected)} \right)^* \right]} \right).$$
 (7)

Intensity and phase differences were fused via complex multiplication to robustly enhance blood flow detection:

$$DP_{i,j,n} = ID_{i,j,n} \exp(i\varphi'_{i,j,n}).$$
 (8)

To further enhance the signal-to-noise ratio (SNR) and suppress artifacts, a split-spectrum processing strategy was employed. The full spectral range was partitioned into M narrow-band subspectra. Each sub-spectrum dataset then underwent independent phase correction and intensity–phase fusion, as described earlier. The results from these M sub-spectra were subsequently averaged to yield the final SSDDPIF angiographic image:

SSDDPIF_{i,j} = 1 -
$$\frac{1}{M(N-1)} \sum_{m=1}^{M} \sum_{n=1}^{N-1} \text{ID}_{i,j,n} \exp\left(i\varphi_{i,j,n}^{\prime(m)}\right)$$
. (9)

We performed OCT angiography (OCTA) imaging of the optic nerve head region in 8-week-old male C57BL/6 mice using a 250 kHz spectral-domain OCT system. Each volumetric dataset comprised 512×400 A-lines, with five repeated B-scans acquired per lateral position without inter-frame registration. The total imaging duration was approximately 4 seconds, using an incident laser power of 1 mW at the cornea. All animals were anesthetized with intraperitoneal injection of tribromoethanol (1.25% in saline, 0.02 mL/g body weight) and mounted on a custom stereotactic holder to minimize motion induced by respiration and cardiac activity.

Previously, we proposed a time-domain phase-intensity fusion (TDPIF) algorithm for OCT angiography that combines phase-sensitive flow detection with intensity information to suppress motion artifacts and improve vascular contrast and SNR [16]. Although TDPIF reduces speckle noise, its sole reliance on time-domain phase correction leaves high-frequency phase fluctuations uncorrected, producing residual bright streaks (Fig. 1(d)).

To overcome this limitation, we developed a dual-domain phase-intensity fusion (DDPIF) angiography. After an initial time-domain phase alignment that removes global low-frequency drift (Eq. (1)), the data are Fourier-transformed and subjected to frequency-domain phase correction (Eq. (4)), substantially attenuating high-frequency streaks while preserving vessel continuity (Fig. 1(e)).

Low-frequency artifacts attributable to bulk-motion—induced intensity fluctuations remain after DDPIF (Fig. 1(e)). We therefore incorporated split-spectrum processing into the dual-domain workflow, resulting in SSDDPIF. Following dual-domain correction, the interferometric spectrum is divided into K Gaussian-windowed sub-bands (Fig. 1(a)). Each sub-band

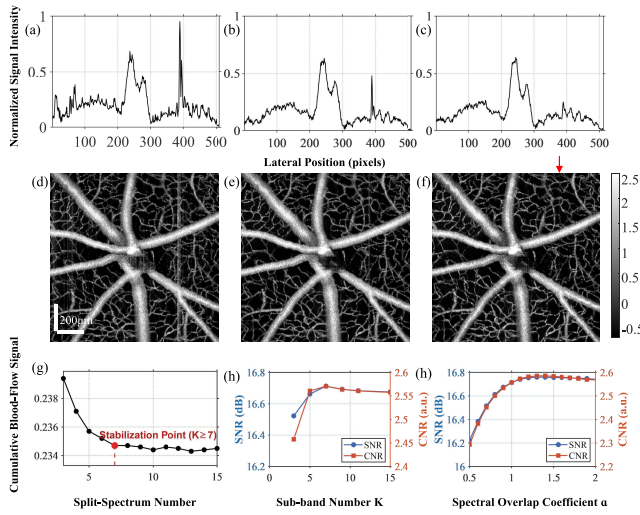


Fig. 1. Quantitative and qualitative evaluation of motion artifact suppression. (a)–(c) Column-wise cumulative blood-flow signal $\sum S(x)$ from *en face* angiograms for (a) TDPIF, (b) DDPIF, and (c) SSDDPIF. Lower peaks indicate better suppression of motion streaks. (d)–(f) Corresponding *en face* angiograms of the same retinal region processed with (d) TDPIF, (e) DDPIF, and (f) SSDDPIF. (g) Cumulative flow signal within the marked ROI plotted against the number of split-spectrum bands ($3 \le K \le 15$), showing a plateau at K = 7. (h) Global SNR and CNR versus sub-band number K (fixed $\alpha = 1.0$). (i) Global SNR and CNR versus spectral overlap coefficient α (fixed K = 7).

is independently calibrated, dispersion-compensated, and reconstructed, after which the sub-band images are averaged to boost SNR and further suppress residual artifacts. The optimal sub-band number was determined by sensitivity analysis (Figs. 1(g) and 1(h)). The cumulative flow-signal intensity decreased with increasing K and plateaued at K = 7, which was adopted in subsequent experiments. We further examined the effect of the spectral overlap coefficient α (Fig. 1(i)), defined as the ratio of the full width at half maximum (FWHM) of each sub-band to the center spacing Δc between adjacent sub-bands (α = FWHM/ Δc). Image quality remained stable near $\alpha \approx 1$.

To benchmark SSDDPIF against established OCTA techniques, we compared it with OMAG, SVOCT, and SSADA. Figure 2 presents cross-sectional OCTA images of the optic nerve head reconstructed by the four algorithms under varying repeatframe conditions (5, 4, 3, and 2 B-scans). Generally, vascular contrast decreases, and background noise and spurious signals become more prominent as the number of repeated B-scans decreases. Under the five-frame condition (Figs. 2(a1)–2(d1)), all methods clearly visualize the capillary network with continuous vessels and high contrast against avascular tissue. When the frame count is reduced to two (Figs. 2(a4)–2(d4)), the image quality markedly deteriorates: microvascular signals appear discontinuous, signal dropout occurs, and speckle noise or false-flow artifacts dominate the background.

Detailed inspection reveals notable differences among algorithms in their robustness to reduced frame numbers. SVOCT) with only two frames (Fig. 2(b4)) produces numerous bright background speckles that could be misinterpreted as vessels, indicating inadequate suppression of static-tissue noise. OMAG (Fig. 2(a4)) retains some vascular contrast but shows elevated

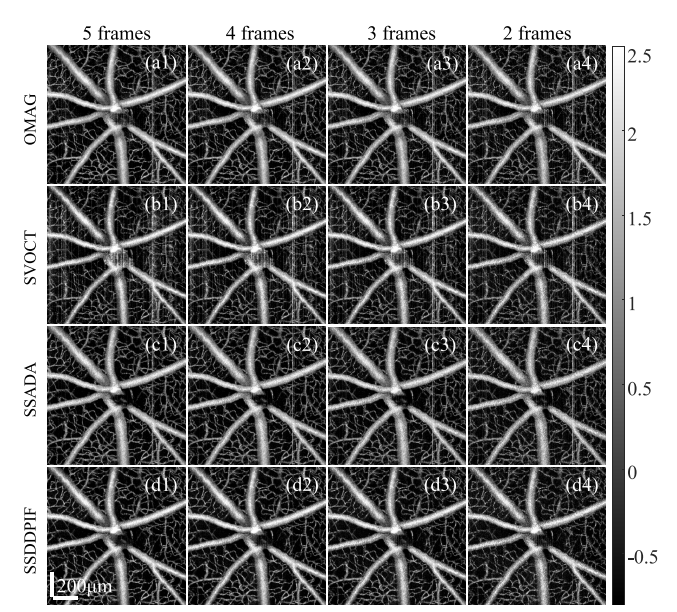


Fig. 2. Cross-sectional OCTA comparison of the optic nerve head. (a) OMAG, (b) SVOCT, (c) SSADA, and (d) SSDDPIF reconstructions. Subpanels 1–4 correspond to 5, 4, 3, and 2 repeated B-scans, respectively.

background noise and blurred vessel edges. In contrast, SSADA maintains clearer vessel contours and lower background noise, primarily due to its use of spectral splitting that reduces interframe noise correlation. Significantly, SSDDPIF demonstrates superior artifact suppression, maintaining clear and continuous vascular structures even at reduced frame counts. This improvement is primarily attributed to its critical frequency-domain phase correction step, which substantially reduces motion-induced high-frequency phase artifacts. Moreover, integrating split-spectrum processing within the SSDDPIF angiography further enhances artifact suppression by decreasing inter-frame noise correlation and improving flow signal fidelity.

All images in this experiment were reconstructed without inter-frame registration, leading to variable motion artifacts across the algorithms. OMAG, SVOCT, and SSADA exhibit pronounced striping or misalignment artifacts at lower frame counts, reflecting insufficient correction for eye motion or system jitter. In contrast, by combining time and frequency-domain phase correction, SSDDPIF effectively mitigates these artifacts and significantly enhances structural coherence, even without motion compensation. Overall, SSDDPIF achieves the highest blood-flow SNR, preserves continuous microvascular networks, and effectively suppresses motion-induced artifacts even when only two repeated frames are available.

To systematically assess the effectiveness of each algorithm in suppressing motion artifacts, a region exhibiting prominent artifacts was selected from the optic nerve head area for quantitative evaluation. Artifact strength was quantified by computing the mean absolute column-wise intensity gradients within each sub-image, serving as a surrogate measure of motion-induced distortions. Higher gradient values correspond to more pronounced edge fluctuations typically associated with uncorrected motion artifacts.

Figure 3(e) summarizes the quantitative results across the selected region for all algorithms. SSDDPIF consistently exhibited the lowest mean gradient, indicating superior suppression of

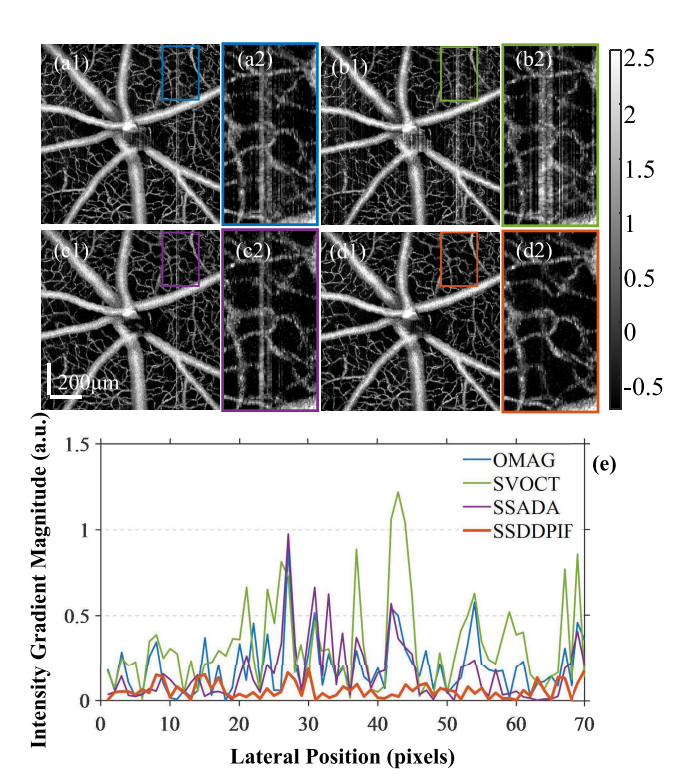


Fig. 3. Local *en face* projection comparison illustrating the effectiveness of motion artifact suppression across algorithms. Left panels (a1)–(d1) display original *en face* projections, while right panels (a2)–(d2) provide enlarged views of regions exhibiting pronounced motion artifacts. (e) Quantitative evaluation of motion artifacts using the mean absolute gradient of OCTA B-scan intensity along the column direction. Images (a1)–(d1) share a common scale bar.

spurious motion-induced vascular signals. Conversely, OMAG and SVOCT demonstrated higher mean gradient, accompanied by distinct streak artifacts. SSADA, while outperforming OMAG and SVOCT, still showed noticeable background interference.

Figure 4 further illustrates algorithm performance under pronounced motion-artifact conditions using the same B-scan slice. Within the region indicated by the red rectangular frame, SSDDPIF (Fig. 4(d2)) maintained the sharpest delineation of capillary lumens and highest vessel-to-background contrast. In contrast, OMAG, SVOCT, and SSADA (Figs. 4(a2)–4(c2)) demonstrated varying degrees of blur, diminishing vascular clarity. Specifically, SVOCT (Fig. 4(b2)) suffered severely from motion-induced blurring, displaying layered tissue structures with minimal discernible vessels. SSADA (Fig. 4(c2)), despite improving upon OMAG and SVOCT, still failed to visualize several microvascular structures clearly. SSDDPIF provided the clearest and most accurate microvascular depiction, significantly surpassing the other algorithms in terms of image quality under motion-affected conditions.

In this Letter, we demonstrated that the proposed SSD-DPIF algorithm effectively suppresses motion artifacts in optic nerve—head OCTA without inter-frame registration. Compared with OMAG, SVOCT, and SSADA, it achieves lower background noise, sharper vessel edges, and more continuous capillary networks, even with only two repeated scans. These results highlight frequency-domain phase correction combined with split-spectrum processing as a practical route to high-contrast,

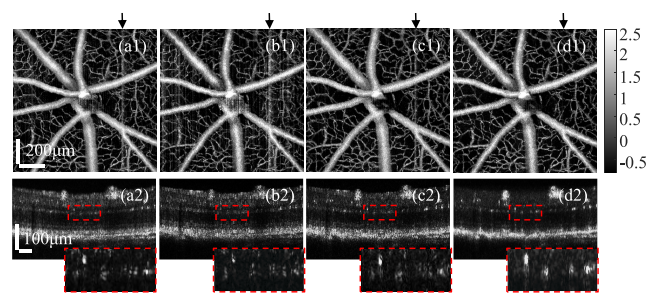


Fig. 4. En face angiograms and corresponding B-scan images of the optic nerve head region obtained using four algorithms, each based on four repeated B-scans at the same lateral position. The top row (a1)–(d1) shows *en face* projections reconstructed by OMAG, SVOCT, SSADA, and SSDDPIF, respectively. The bottom row (a2)–(d2) presents the corresponding B-scan images. All panels are displayed with consistent lateral scale bars (200 µm for *en face* projections and corresponding lateral spans for B-scans).

motion-robust OCTA in fast volumetric imaging. Although validated in mice, translation to human imaging will require strategies to address stronger eye motion, thicker retinal layers, and intersubject variability, as well as large-scale clinical validation. With GPU acceleration, SSDDPIF achieves practical processing times, underscoring its feasibility for extended preclinical studies and potential clinical applications.

Funding. National Natural Science Foundation of China (62205181); Natural Science Foundation of Shandong Province (ZR2022QF017); Shandong Province Outstanding Youth Science Fund Project (Overseas) (2023HWYQ-023); Taishan Scholar Foundation of Shandong Province (tsqn202211038); Key Technology Research and Development Program of Shandong Province (2024CXGC010106).

Disclosures. The authors declare no conflicts of interest.

Data availability. Data underlying the results presented in this paper are not publicly available at this time but may be obtained from the authors upon reasonable request.

Supplemental document. See Supplement 1 for supporting content.

REFERENCES

- 1. D. Huang, E. A. Swanson, C. P. Lin, et al., Science 254, 1178 (1991).
- R. F. Spaide, J. G. Fujimoto, N. K. Waheed, et al., Prog. Ret. Eye Res. 64, 1 (2018).
- S. R. Sadda, R. Guymer, F. G. Holz, et al., Ophthalmology 125, 537 (2018).
- 4. W. Song, S. Fu, S. Song, et al., Neurophotonics 6, 041103 (2019).
- 5. Z. Sun, F. Tang, R. Wong, et al., Ophthalmology 126, 1675 (2019).
- J. Scholler, Opt. Express 27, 19562 (2019).
- J. Lee, V. Srinivasan, H. Radhakrishnan, et al., Opt. Express 19, 21258 (2011).
- 8. S. Makita, M. Miura, S. Azuma, *et al.*, Biomed. Opt. Express **12**, 637
- 9. L. Pan and X. Chen, IEEE Rev. Biomed. Eng. 16, 307 (2021).
- A. Mariampillai, B. A. Standish, E. H. Moriyama, *et al.*, Opt. Lett. **33**, 1530 (2008).
- R. K. Wang, S. L. Jacques, Z. Ma, et al., Opt. Express 15, 4083 (2007).
- 12. Y. Jia, O. Tan, J. Tokayer, et al., Opt. Express 20, 4710 (2012).
- 13. R. de Kinkelder, J. Kalkman, D. J. Faber, et al., Invest. Ophthalmol. Vis. Sci. 52, 3908 (2011).
- 14. H. Li, K. Liu, T. Cao, et al., Opt. Lett. 46, 368 (2021).
- 15. W. Yi, K. Hu, Y. Wan, et al., J. Lumin. 270, 120550 (2024).
- 16. F. Wu, X. He, Y. Li, et al., Opt. Lett. 50, 4286 (2025).